ChemComm
Chemical Communications

Accepted Manuscript

This article can be cited before page numbers have been issued, to do this please use: Z. Liu, F. Guo, M. Li, S. Jiang, X. Lang, A. Dutta Chowdhury and K. Cheng, *Chem. Commun.*, 2026, DOI: 10.1039/D6CC03041F.




ROYAL SOCIETY OF CHEMISTRY

rsc.li/chemcomm

ROYAL SOCIETY OF CHEMISTRY View Article Online
DOI: 10.1039/D6CC03041F

ChemComm

COMMUNICATION

# Sodium-promoted bimetallic *M*-$CoO_x$ catalysts (*M* = In, Ga, Mo, Mn, and V) for the hydrogenation of $CO_2$ to $C_{2+}$ hydrocarbons

Received 00th January 20xx,
Accepted 00th January 20xx,

DOI: 10.1039/x0xx00000x

www.rsc.org/

Zuozheng Liu,[a] Furan Guo,[b] Miao Li,[b] Shican Jiang,[a] Xianjun Lang,*[a] Abhishek Dutta Chowdhury,*[a] and Kang Cheng*[b]



**In $CO_2$ hydrogenation, Na-V-modified cobalt nanoparticles redirect the product distribution from methane to $C_{2+}$ hydrocarbons. Sodium facilitates C–C chain propagation and suppresses methanation reaction, while vanadium enhances site dispersion and regulates the $Co^0/Co^{\delta+}$ ratio, collectively driving the coupled reverse water–gas shift and Fischer–Tropsch synthesis reactions.**

Driven by green hydrogen technology, the utilization of $CO_2$ as a carbon feedstock offers a sustainable route to carbon-based fuels and chemicals.[1-3] Co-based catalysts are widely applied in Fischer–Tropsch (FT) synthesis due to their high chain-growth capability.[4,5] However, in $CO_2$ hydrogenation, Co-based catalysts often catalyze the formation of light alkanes, especially $CH_4$.[6,7] Studies on CO and $CO_2$ hydrogenation over Co-based catalysts indicate that $Co^0$ favours $H_2$ dissociation and C–C coupling, whereas $Co^{\delta+}$ sites ($0 \leq \delta \leq 3$) enhance $CO_2$ adsorption and facilitate the production of CO by reverse water–gas shift (RWGS) reaction.[8-11] Therefore, tuning the chemical environment of Co could potentially regulate the product selectivity towards more valuable products in $CO_2$ hydrogenation, such as $C_{2+}$ hydrocarbons ($C_{2+}H$).

Introducing a second metal offers an effective way to tailor the geometric and electronic structures of Co sites, thereby adjusting the product distribution of $CO_2$ hydrogenation. Wang et al. found an in situ produced $Cu^0$-$Co_2C$ interface that facilitated CO insertion and exhibited a $C_{2+}H$ selectivity of 60% at 300 °C.[12] Bibi et al. developed a $Co^0$ core and $ZrO_2$ shell architecture that stabilized Co nanoparticles (NPs) and offered a $C_{2+}H$ selectivity of 57% at $CO_2$ conversion of 70%.[13] Jo et al. reported a Na and Mn co-promoted core-shell Co@$CoO_x$/$Co_2C$ catalyst, in which the Mn-induced $CoO_x$ shell suppressed excessive methanation, enabling a $C_{5+}H$ yield of 21%.[14] The addition of alkali promoters has also been demonstrated to adjust surface C/H coverage on Co sites, thus tuning the hydrocarbon selectivities.[15,16]

Although several bimetallic Co-based catalysts have shown promise for $CO_2$ to $C_{2+}H$ conversion, the catalyst library remains narrow, and the factors governing $C_{2+}H$ selectivity are still underexplored. Herein, we investigate the synergistic mechanism and structural modulation of Na-*M*-$CoO_x$ catalysts (*M* = In, Ga, Mo, Mn, and V, Na = 1.0 wt%, *M* = 1.0 wt%) for $CO_2$ hydrogenation to $C_{2+}H$. Under 250 °C and 3 MPa, the optimum Na-1V-$CoO_x$ catalyst achieves a $C_{2+}H$ selectivity of 63% at a $CO_2$ conversion of 30%, close to the performance of benchmark catalysts reported in this area (Table S1, ESI†). The structure-activity relationship has been proposed based on a series of characterizations.

The *M*-$CoO_x$ was synthesized by a urea-assisted hydrothermal precipitation method (see the ESI† for experimental details). Pristine $CoO_x$ catalyst, obtained by reducing $Co_3O_4$ at 300 °C for 2 h, gave a $CO_2$ conversion of 42% and a $CH_4$ selectivity of 93% (Figure 1a). The introduction of Na with only 1.0 wt% amount significantly influenced the catalytic performance, with the $CO_2$ conversion decreased to 15%. However, the $CH_4$ selectivity was suppressed to 39%, and the $C_{2+}H$ and $C_{5+}H$ selectivities were increased to 61% and 34%, respectively. The chain growth probability (α) of Na-$CoO_x$ was estimated to be 0.71 (Figure S1, ESI†). The CO selectivity was only 6.5%. Generally, the combination of Na-$CoO_x$ with In, Ga, Mo, Mn, and V didn't change the product distribution significantly, but the $CO_2$ conversion. Among them, Na-In-$CoO_x$ exhibited a $CO_2$ conversion of 17% with the $C_{2+}H$ selectivity of 54%. Na-Ga-$CoO_x$ achieved a $CO_2$ conversion of 18% with the $C_{2+}H$ selectivity of 62%. Na-Mo-$CoO_x$ delivered a $CO_2$ conversion of 24% with the $C_{2+}H$ selectivity of 66%, but the CO selectivity increased to 11%. Na-Mn-$CoO_x$ exhibited a $CO_2$ conversion of 28% with the $C_{2+}H$ selectivity of 61%.

Na-V-$CoO_x$ afforded the optimum promotional effect with $CO_2$ conversion of 30% and $C_{2+}H$ selectivity of 63%. The $C_{2+}H$ yield and space time yield (STY) were 19% and 12 $mmol \cdot g_{cat}^{-1} \cdot h^{-1}$, respectively. The selectivity of liquid hydrocarbons ($C_{5+}H$) was 37%. Besides, CO selectivity was only 1.8%, significantly lower than that over Fe-based and Ru-based catalysts in $CO_2$ hydrogenation.[17,18] Overall, V serves as an effective promoter for Na-Co-based catalysts in $CO_2$

[a] College of Chemistry and Molecular Sciences, Wuhan University, Wuhan 430072, China. E-mail: 2023102030032@whu.edu.cn, xianjunlang@whu.edu.cn, abhishek@whu.edu.cn
[b] State Key Laboratory of Physical Chemistry of Solid Surfaces, Innovation Laboratory for Science and Technologies of Energy Material of Fujian Province (IKKEM), College of Chemistry and Chemical Engineering, Xiamen University, Xiamen 361005, China. E-mail: kangcheng@xmu.edu.cn

View Article Online
DOI: 10.1039/D6CC00415





hydrogenation to enhance the formation of desired $C_{2+}H$ product. We further investigated the V loading and found that a loading of 1.0 wt% was optimum for the formation of $C_{2+}H$ (Figure S2, ESI†). With the V loading increased to 5.0 wt%, the $CO_2$ conversion decreased to 25%, while the selectivities for CO and $C_{2+}H$ remained nearly constant. For Na-10V-$CoO_x$, although the $C_{2+}H$ selectivity increased to 74%, the $CO_2$ conversion dropped sharply to 6.5%. Besides, the CO selectivity increased to 35%. The activation energies ($E_a$) calculated on $C_{2+}H$ STY at varying reaction temperatures (Figures S3, ESI†) suggest that the introduction of 1.0wt% V markedly reduced the $E_a$ from 93 to 62 kJ·mol$^{-1}$. However, if the V loading was increased to 10 wt%, the $E_a$ was 76 kJ·mol$^{-1}$. This trend generally agrees well with the catalyst reactivity in $CO_2$ hydrogenation (Figures S2, ESI†). We evaluated the stability of both Na-1V-$CoO_x$ and Na-$CoO_x$ catalysts (Figure 1b and S4, ESI†). During 70 h on stream, Na-1V-$CoO_x$ exhibited significantly better stability than Na-$CoO_x$, especially in product distribution. The $C_{2+}H$ STY of Na-1V-$CoO_x$ decreased slightly from 12 to 9.5 mmol·$g_{cat}^{-1}$·h$^{-1}$, whereas Na-$CoO_x$ deactivated more severely, with $C_{2+}H$ STY dropping from 7.4 to 3.8 mmol·$g_{cat}^{-1}$·h$^{-1}$.

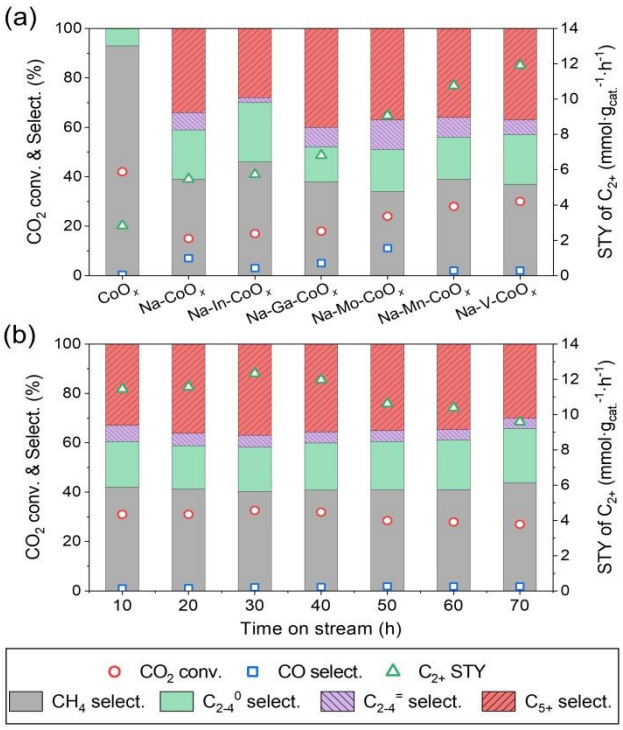


**Fig. 1** (a) Catalytic performance of $CO_2$ hydrogenation over $CoO_x$ and Na-*M*-$CoO_x$ (*M* = In, Ga, Mo, Mn, and V, Na = 1.0 wt%, *M* = 1.0 wt%) catalysts. (b) Stability of Na-1V-$CoO_x$. Reaction conditions: 0.1 g, 250 °C, $H_2/CO_2$ = 3, 3 MPa, 6000 mL·$g_{cat}^{-1}$·h$^{-1}$. $C_{2-4}^0$ and $C_{2-4}^=$ denote $C_2$–$C_4$ alkanes and $C_2$–$C_4$ olefins, respectively.

The reaction kinetics have been investigated over the optimal Na-1V-$CoO_x$ catalyst. Raising the reaction temperature from 210 to 290 °C increased $CO_2$ conversion from 5.8% to 66% and decreased CO selectivity from 7.9% to 0.5% (Figure 2a), indicating that a higher temperature is favourable for $CO_2$ activation and CO consumption. However, higher temperatures also shifted product selectivity from $C_{2+}H$ to $CH_4$. Catalytic performance is strongly dependent on reaction pressures (Figure 2b). With the pressure increased from 1 to 4 MPa, the $CO_2$ conversion rose from 14% to 34%, while the CO selectivity decreased from 11% to 1.1%. These trends indicate that the consumption of CO intermediates likely follows the FT synthesis mechanism. Meanwhile, the $C_{2+}H$ selectivity remained nearly constant at 63–65% in the pressure range of 1–3 MPa, then gradually decreased to 56% at 4 MPa, suggesting that high pressure favors the deep hydrogenation of CO-derived intermediates.

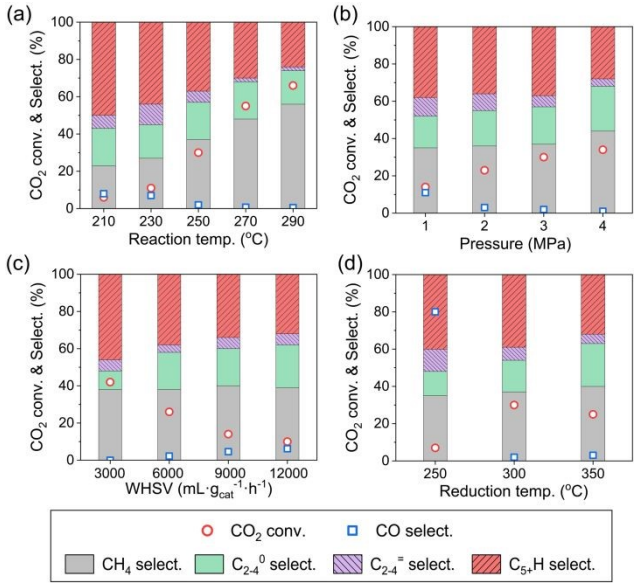


**Fig. 2** Catalytic performance of Na-1V-$CoO_x$ catalyst. (a) Effect of reaction temperature. Reaction condition: 0.1 g, 210–290 °C, $H_2/CO_2$ = 3, 3 MPa, 6000 mL·$g_{cat}^{-1}$·h$^{-1}$. (b) Effect of pressures. Reaction conditions: 0.1 g, $H_2/CO_2$ = 3, 250 °C, 1–4 MPa, 6000 mL·$g_{cat}^{-1}$·h$^{-1}$. (c) Effect of WHSV. Reaction condition: 0.1 g, 250 °C, $H_2/CO_2$ = 3, 3 MPa, 3000–12000 mL·$g_{cat}^{-1}$·h$^{-1}$. (d) Effect of reduction temperature. Reaction conditions: 0.1 g, $H_2/CO_2$ = 3, 250 °C, 3 MPa, 6000 mL·$g_{cat}^{-1}$·h$^{-1}$.

To probe the reaction pathway, we evaluated Na-1V-$CoO_x$ at different weight hourly space velocities (WHSV) (Figure 2c). As the WHSV increased from 3000 to 12000 mL·$g_{cat}^{-1}$·h$^{-1}$, the $CO_2$ conversion decreased from 42% to 10%, while CO selectivity rose from 0 to 6.0%, indicating that shorter residence time limits the conversion of CO. $C_{2+}H$ selectivity was not affected, but $C_{5+}H$ selectivity decreased from 46% to 32% as the WHSV increased from 3000 to 12000 mL·$g_{cat}^{-1}$·h$^{-1}$, and the olefin/paraffin (o/p) ratio decreased from 0.6 to 0.3 (Table S2, ESI†). This implies a $CO_2$ → CO → $C_{2+}H$ → $C_{5+}H$ pathway. Since the redox state of Co may influence the hydrogenation behavior, we then assessed the impact of reduction conditions on the $CO_2$ hydrogenation over Na-1V-$CoO_x$ (Figure 2d). At the reduction temperature of 250 °C, the $CO_2$ conversion was only 7.0% with a high CO selectivity of 80%. This implies that Co-based catalysts in an oxidized state preferentially catalyze the RWGS reaction, and the formed CO cannot be efficiently consumed for C–C chain growth. As the reduction temperature increased to 300 °C, the reactivity of $CO_2$ hydrogenation increased significantly. However, further increasing the reduction temperature to 350 °C lowered the $CO_2$ conversion to 25%, along with the increase of $CH_4$ and $C_{2-4}^0$ selectivities. Generally, $C_{2+}H$ selectivity decreases as the $CO_2$ conversion increases, while $CH_4$ selectivity

 

follows an inverse trend according to statistics of all catalytic results (Figure S5 and Table S2, ESI†). Compared with reported Co-based and Fe-based catalysts, which were typically evaluated in a high temperature range of 270–350 °C to sustain high $C_{2+}H$ STY, our catalyst achieves a comparable $C_{2+}H$ yield and STY under relatively mild conditions (Table S1, ESI†).

We performed a series of characterizations to elucidate the physicochemical properties of Co-based catalysts. The ICP-OES analysis evidences that the Na-promoted catalysts have similar Na loadings of 0.9 wt%, and V-promoted catalysts have V loadings of about 0.9 and 9.5 wt%, respectively (Table S3, ESI†), which are close to their dosages in catalyst preparation. XRD analysis shows that all samples exhibit diffraction peaks corresponding to $Co_3O_4$ (Figure S6, ESI†). Notably, no discernible diffraction peaks for crystalline $VO_x$ or Na species were observed, suggesting that V and Na are highly dispersed. Based on the primary reflection at 2θ = 36.9°, assigned to the $Co_3O_4$ (311) plane, and using the Scherrer equation, the crystallite sizes were estimated to be 55, 35, and 30 nm for Na-$CoO_x$, Na-1V-$CoO_x$, and Na-10V-$CoO_x$, respectively. This indicates that V incorporation can reduce the catalyst crystallite size (Table S3, ESI†). $N_2$ physisorption reveals a type IV isotherm with hysteresis loops for all the catalysts, indicating mesoporous structures arising from interparticle space (Figure S7 and Table S3, ESI†). With the increase of V loading, the surface area and pore volume rise from 11 $m^2 \cdot g^{-1}$/0.1 $cm^3 \cdot g^{-1}$ (Na-$CoO_x$) to 18 $m^2 \cdot g^{-1}$/0.1 $cm^3 \cdot g^{-1}$ (Na-1V-$CoO_x$) and 32 $m^2 \cdot g^{-1}$/0.2 $cm^3 \cdot g^{-1}$ (Na-10V-$CoO_x$). SEM reveals that Na-$CoO_x$ shows a layered morphology with densely packed, relatively large NPs and limited interparticle space (Figure 3a–c). Introducing V partially disrupts the layered framework and yields smaller particles in the form of bundle-like aggregates, which is consistent with the increased BET surface area and pore volume.

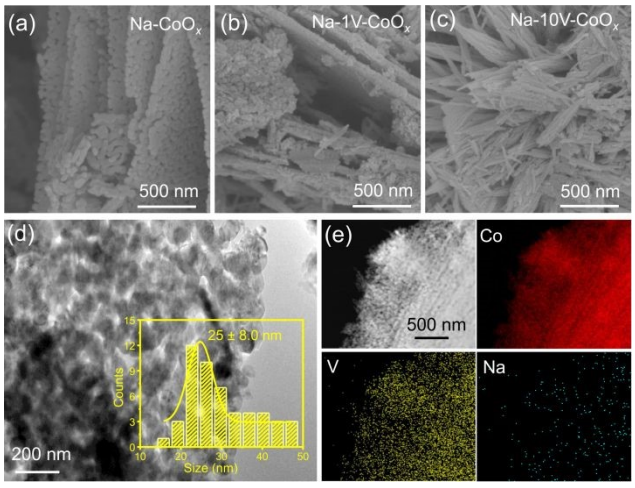


**Fig. 3** SEM images of (a) Na-$CoO_x$, (b) Na-1V-$CoO_x$, and (c) Na-10V-$CoO_x$ catalysts. (d) TEM image of Na-1V-$CoO_x$. (e) HAADF-STEM image and EDS mapping of Na-1V-$CoO_x$ catalyst.

Ultraviolet–visible spectroscopy (UV-vis) shows that the three catalysts exhibit similar spectral features, with a strong 200–400 nm Co–O charge-transfer band and a broad 600–800 nm $Co^{2+}$ *d–d* band (Figure S8, ESI†).[19] Compared with Na-$CoO_x$, V-containing samples show a red shift of the shoulder, suggesting that dispersed $VO_x$ modulates the local Co electronic structure.[20] To analyse the crystalline phases and elemental distributions, we performed HRTEM and STEM-EDS mapping on the three catalysts. For Na-$CoO_x$, the average size of Co NPs is 37 nm, and the lattice spacing of 0.25 nm corresponds to the (311) plane of $Co_3O_4$ (Figure S9a–c, ESI†). After introducing 1.0 wt% V, the particle size decreases to 25 nm (Figure 3d and Table S3, ESI†). Meanwhile, EDS mapping reveals a homogeneous distribution of V and Na (Figure 3e). When the V loading is further increased to 10 wt%, the particle size decreases to 21 nm, and $Co_3O_4$ lattice planes such as (311) and (220) can be observed, whereas V-related species remain highly dispersed (Figure S9d–f, ESI†).

$H_2$ temperature-programmed reduction ($H_2$-TPR) reveals the role of V loading in tuning the reduction behavior of Co species (Figure S10, ESI†). Na-$CoO_x$ exhibits the typical reduction peaks at 343 °C ($Co^{3+} \rightarrow Co^{2+}$) and 408 °C ($Co^{2+} \rightarrow Co^0$).[21] Both Na-1V-$CoO_x$ and Na-10V-$CoO_x$ show broadened and prolonged reduction peaks, and the peak area is smaller than that of Na-$CoO_x$, indicating that V doping suppresses the overall reducibility of Co species. The reduction degrees of Na-$CoO_x$, Na-1V-$CoO_x$, and Na-10V-$CoO_x$, as estimated from $H_2$ consumption at 300 °C, are 74%, 53%, and 33%, respectively (Figure S11 and Table S3, ESI†). This indicates that the Co exists in a mixed-valence state of $Co^0$ and $Co^{\delta+}$ after reduction. This is also the reason that the cobalt catalyst is named as $CoO_x$ in this work.

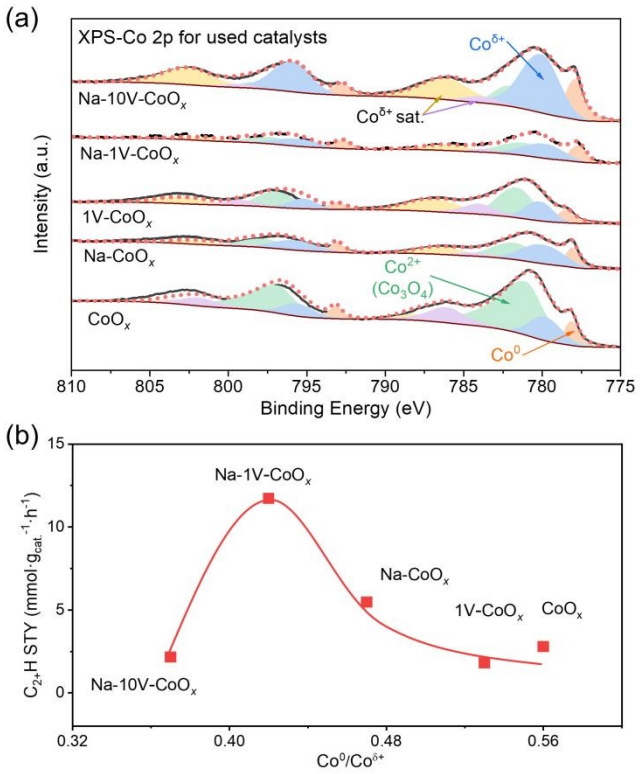


**Fig. 4** (a) Co 2p XPS of the used Na-*y*V-$CoO_x$ catalysts (*y* = 0, 1, and 10 wt%) after reaction for 18 h. (b) Correlation of $C_{2+}H$ formation rates and surface $Co^0/Co^{\delta+}$ ratios.

XRD analysis for reduced catalysts suggests that Na-$CoO_x$ contains both CoO and $Co^0$, indicating partial reduction of $Co_3O_4$

(Figure S12, ESI†). With 1.0 wt% V added, CoO and $Co^0$ still coexist, but the $Co^0$ peaks weaken, indicating V suppresses the reduction of Co oxides. The absence of V-related diffraction peaks implies that V remains highly dispersed after reduction. For Na-10V-$CoO_x$, the CoO peaks become broader and weaker, and the $Co^0$ peak is almost absent. XRD patterns of the used catalysts reveal their structural evolution and stability under reaction conditions (Figure S13, ESI†). After reaction, Na-$CoO_x$ is dominated by $Co^0$. Na-1V-$CoO_x$ exhibits much weaker and broadened characteristic diffraction of $Co^0$, with the 42–45° peaks shifting to higher 2θ values than Na-$CoO_x$, indicating lattice contraction in Co domains likely caused by lattice distortion.[22] For used Na-10V-$CoO_x$, CoO, and weak metallic $Co^0$ reflections are observed, indicating that high V loading suppresses the reduction of Co species.

To elucidate the surface chemistry of used catalysts, X-ray photoelectron spectroscopy (XPS) was performed (Figure 4a and Table S4, ESI†). Deconvolution of Co 2p reveals the presence of $Co^0$ (778.1 eV), $Co^{\delta+}$ (779.9 eV), and $Co^{2+}$ ($Co_3O_4$) (781.2 eV) in all samples.[13,14,23] According to the literature, oxidized Co species ($Co^{\delta+}$) are generally regarded as active for RWGS, whereas $Co^0$ provides for C–C coupling in FT synthesis.[5,6] On this basis, we then examined how the $Co^0/Co^{\delta+}$ ratio correlates with catalytic performance. A volcano-shaped relationship is observed when the XPS-derived $Co^0/Co^{\delta+}$ peak-area ratio is plotted against the $C_{2+}$H STY. At low $Co^0/Co^{\delta+}$ ratios, the formation of CO by RWGS reaction is favoured, while at high $Co^0/Co^{\delta+}$ ratios, methanation reaction dominates the reaction process (Figure 4b and Table S5, ESI†).

In situ DRIFTS was performed to probe surface intermediates and reaction pathways during $CO_2$ hydrogenation (Figure S14, ESI†). Upon introducing the $CO_2/H_2$, a series of carbon-oxygen species were observed, including carbonate (*$CO_3^{2-}$, 1400–1460 $cm^{-1}$), bicarbonate (*$HCO_3^-$, 1500/1650 $cm^{-1}$), carboxyl (*COOH, 1700–1760 $cm^{-1}$), CO (2100–2200 $cm^{-1}$), and $CH_x$ (C–H stretching at 3000 $cm^{-1}$) species.[24,25] Compared with Na-$CoO_x$ and Na-1V-$CoO_x$, Na–10V–$CoO_x$ exhibits much stronger carbonate, bicarbonate, and carboxyl signals, indicating its weaker hydrogenation ability, which is consistent with its low reactivity in $CO_2$ hydrogenation (Figure S1, ESI†). Combined with reaction kinetic data (Figure 2), we speculate that $CO_2$ is first hydrogenated to CO via the bicarbonate/carboxyl route on $Co^{\delta+}$ sites. The generated CO is immediately consumed for $CH_x$ formation and C–C coupling (FT synthesis) on the adjacent $Co^0$ sites. Therefore, the balance between $Co^0/Co^{\delta+}$ is critical to determining the density of surface intermediates and final products.

In summary, we obtained an optimized Na-1V-$CoO_x$ catalyst, offering $CO_2$ conversion of 30% with $C_{2+}$H selectivity of 63% at 250 °C, and 3 MPa. The CO selectivity was only 1.8%. The introduction of V has been evidenced to suppress particle growth, leading to smaller Co domains and increased surface area. Besides, Na and V electronically modulate the electron density of Co, stabilizing an appropriate surface $Co^0/Co^{\delta+}$ ratio that balances the RWGS and FT synthesis steps. This balanced interplay enables efficient C–C coupling and significantly enhances the production of value-added $C_{2+}$ hydrocarbons.

## Conflicts of interest

There are no conflicts to declare.

## Data availability

The data supporting this article are included in this file and in the supplementary information. Supplementary information includes experimental procedures, additional characterization, catalysis, and analysis data. See DOI: https://doi.org/10.1039/x.

## Acknowledgements

This work was supported by the National Key Research and Development Program of Ministry of Science and Technology (No. 2022YFA1504600), the National Natural Science Foundation of China (Nos. 22121001, U25B6005, and 22572150), the Fujian Provincial Natural Science Foundation of China (2026J011001), the Fundamental Research Funds for the Central Universities (20720250081), and the Open Project of State Key Laboratory of Physical Chemistry of Solid Surfaces (No. 202102).

## Notes and references

1 R. Ye, J. Ding, T. R. Reina, M. S. Duyar, H. Li, W. Luo, R. Zhang, M. Fan, G. Feng, J. Sun and J. Liu, *Nat. Synth.*, 2025, **4**, 288-302.
2 K. Cheng, Y. Li, J. Kang, Q. Zhang and Y. Wang, *Acc. Chem. Res.*, 2024, **57**, 714-725.
3 J. Ye, N. Dimitratos, L. M. Rossi, N. Thonemann, A. M. Beale and R. Wojcieszak, *Science*, **387**, eadn9388.
4 K. Cheng, J. Kang, D. L. King, V. Subramanian, C. Zhou, Q. Zhang and Y. Wang, *Adv. Catal.*, 2017, **60**, 125-208.
5 A. Y. Khodakov, W. Chu and P. Fongarland, *Chem. Rev.*, 2007, **107**, 1692-1744.
6 M. Wang, G. Zhang, J. Zhu, W. Li, J. Wang, K. Bian, Y. Liu, F. Ding, C. Song and X. Guo, *Chem. Eng. J.*, 2022, **446**, 137217.
7 G. Melaet, W. T. Ralston, C.-S. Li, S. Alayoglu, K. An, N. Musselwhite, B. Kalkan and G. A. Somorjai, *J. Am. Chem. Soc.*, 2014, **136**, 2260-2263.
8 X. Zhou, G. A. Price, G. J. Sunley and C. Copéret, *Angew. Chem. Int. Ed.*, 2023, **135**, e202314274.
9 K. Li, X. Li, L. Li, X. Chang, S. Wu, C. Yang, X. Song, Z.-J. Zhao and J. Gong, *JACS Au*, 2023, **3**, 508-515.
10 A. Parastaev, V. Muravev, E. H. Osta, T. F. Kimpel, J. F. M. Simons, A. J. F. van Hoof, E. Uslamin, L. Zhang, J. J. C. Struijs, D. B. Burueva, E. V. Pokochueva, K. V. Kovtunov, I. V. Koptyug, I. J. Villar-Garcia, C. Escudero, T. Altantzis, P. Liu, A. Béché, S. Bals, N. Kosinov and E. J. M. Hensen, *Nat. Catal.*, 2022, **5**, 1051-1060.
11 I. C. t. Have, J. J. G. Kromwijk, M. Monai, D. Ferri, E. B. Sterk, F. Meirer and B. M. Weckhuysen, *Nat. Commun.*, 2022, **13**, 324.
12 M. Wang, S. Guo, S. Yan, Z. Wang, G. Zhang, H. Gao, M. Zhang, K. Bian, J. Liu, X. Nie, J. Zeng, C. Song and X. Guo, *J. Am. Chem. Soc.*, 2025, **147**, 42051-42060.
13 S. S. Bibi, H. Jo, J. R. Sugiarto, S. Ahmed, M. Irshad, W. Yoon and J. Kim, *J. Energy Chem.*, 2025, **108**, 769-784.
14 H. Jo, H.-J. Chun, J. R. Sugiarto, M. K. Khan, M. Irshad, W. Yoon, S. K. Kim and J. Kim, *Appl. Catal. B: Environ.*, 2024, **359**, 124457.
15 Z. Shi, H. Yang, P. Gao, X. Li, L. Zhong, H. Wang, H. Liu, W. Wei and Y. Sun, *Catal. Today*, 2018, **311**, 65-73.
16 Z. Shi, H. Yang, P. Gao, X. Chen, H. Liu, L. Zhong, H. Wang, W. Wei and Y. Sun, *Chin. J. Catal.*, 2018, **39**, 1294-1302.
17 Z. Liu, F. Guo, L. Ge, S. Jiang, X. Lang, A. Dutta Chowdhury, Y. Zheng, K. Cheng and Y. Wang, *Energy Fuels*, 2025, **39**, 20957-20965.



 

View Article Online
DOI: 10.1039/D6CC03041F

18 Q. Yang and E. V. Kondratenko, *Acc. Mater. Res.*, 2024, **5**, 1314-1328.
19 A. B. Vennela, D. Mangalaraj, N. Muthukumarasamy, S. Agilan and K. V. Hemalatha, *Int. J. Electrochem. Sci.*, 2019, **14**, 3535-3552.
20 S. Farhadi, J. Safabakhsh and P. Zaringhadam, *J. Nanostruct. Chem.*, 2013, **3**, 69.
21 K. Cheng, V. Subramanian, A. Carvalho, V. V. Ordomsky, Y. Wang and A. Y. Khodakov, *J. Catal.*, 2016, **337**, 260-271.
22 R. D. Shannon and C. T. Prewitt, *Acta Crystallogr. B*, 1969, **25**, 925-946.
23 S. Zhang, K. An, J. Xin, Y. Jiang, M. Niu, P. Song, C. Wu, H. Wang and Y. Liu, *Chem. Eng. J.*, 2024, **486**, 150334.
24 W. Yu, M. Zhu, Z. Yang and Y.-F. Han, *ACS Catal.*, 2025, **15**, 3428-3441.
25 M. Wang, L.-C. Wang, B. Liu, Y. Ding, Y. Yang and D. Ding, *ACS Catal.*, 2025, **15**, 5954-5967.



View Article Online
DOI: 10.1039/D6CC03041F

The data supporting this article are included in this file and in the supplementary information. Supplementary information includes experimental procedures, additional characterization, catalysis, and analysis data. See DOI: https://doi.org/10.1039/x.